Study on debinding and sintering conditions in extrusion-based additive manufacturing of 316L and 316L + Cu

Jean-François Silvain, Daniel Lincoln Gifford, Sébastien Fourcade, Laurent Cuzacq, Jean-Luc Grosseau-Poussard, Catherine Debiemme-Chouvy, Nicolas Tessier Doyen, Yongfeng Lu

Article

Study on Debinding and Sintering Conditions in Extrusion-Based Additive Manufacturing of 316L and 316L + Cu

Jean-François Silvain [1,2,*], Daniel Lincoln Gifford [1], Sébastien Fourcade [1], Laurent Cuzacq [1], Jean-Luc Grosseau-Poussard [3], Catherine Debiemme-Chouvy [4], Nicolas Tessier Doyen [5] and Yongfeng Lu [2]

1. Bordeaux Institute of Condensed Matter Chemistry, University of Bordeaux, CNRS, Bordeaux INP, ICMCB, UMR 5026, 87 Av. Dr. A. Schweitzer, 33600 Pessac, France; dgifford17@gmail.com (D.L.G.); sebastien.fourcade@icmcb.cnrs.fr (S.F.); laurent.cuzacq@icmcb.cnrs.fr (L.C.)
2. Department of Electrical and Computer Engineering, University of Nebraska-Lincoln, Lincoln, NE 68588-0511, USA; yflu.email@gmail.com
3. LaSie, Pole Science et Technologie, Université de La Rochelle, Av. M. Crépeau, 17042 La Rochelle, France; jlgrouss@univ-lr.fr
4. Laboratoire Interfaces et Systèmes Electrochimiques, UMR 8235 CNRS—SU, Sorbonne Université, CNRS, 4 Place Jussieu, 75005 Paris, France; catherine.debiemme-chouvy@sorbonne-universite.fr
5. IRCER, Institute of Research for Ceramics, IRCER, CNRS, Université de Limoges, CEC, 12 Rue Atlantis, 87068 Limoges, France; nicolas.tessier-doyen@unilim.fr
* Correspondence: jean-francois.silvain@icmcb.cnrs.fr

Abstract: This study investigates the use of a methylcellulose binder in extrusion additive manufacturing of 316L as an alternative to common wax-based binders. Various quantities of copper (Cu) powder were also added in the paste composition to attempt to reduce the sintering temperature by promoting persistent liquid phase sintering. Debinding experiments were conducted under different temperatures and dwell times using argon (Ar), Ar/5%H_2, and Ar/1%O_2 atmospheres. Debinding reduced carbon (C) content to 0.032 wt.% by using a two-step debinding process of Ar/5%H_2 and Ar/1%O_2 thermal treatments. Using this debinding process, sintering was conducted at 1200 °C under Ar/5%H_2 atmosphere with the presence of 0, 10, and 20 vol.% Cu in the paste. Microstructure, mechanical, and corrosion properties were studied. Cu additions allowed the improvement of the densification when sintering at 1200 °C was performed. A 20 vol.% Cu addition yielded 88% relative density after sintering for 10 h, while pure 316L powder sintered under the same conditions had 70%. Mechanical properties were inferior to fully dense stainless steel, but it is not clear if this is due to the Cu additions or insufficient densification.

Keywords: additive manufacturing; 316L; copper; organic paste; mechanical properties

1. Introduction

Additive manufacturing (AM), also known as 3D printing, allows users to rapidly create complex parts without the limitations of traditional shaping and forming processes [1,2]. It uses computer-aided design (CAD) data to build parts with intricate detail and minimal waste. Extrusion-based additive manufacturing (EAM) is a technique that extrudes material through the nozzle of a toolhead onto a platform to form the desired part [3–5]. This technique is seen as a combination of two separate techniques: fused deposition modeling [6] and metal injection molding [7]. Fused deposition modeling (FDM) draws a thermoplastic filament through a heated nozzle using a stepper motor to form polymeric 3D parts. Metal injection molding (MIM) mixes fine metal powder with a polymer binder to form a slurry which is then pumped into a mold to form the part [5,8]. EAM uses the same equipment as FDM but has a toolhead with a syringe attachment which pumps a metal/binder slurry and deposits strands of the material onto a platform layer by layer to form the final part. Interest in this process stems from its cost efficiency when compared to other AM processes. Metallic additive manufacturing techniques often include high-energy arcs and beams and

may also require high-temperature environments. For these reasons, companies would be required to invest large capital to apply this technology. Conversely, the EAM process is commonly printed close to room temperature with much lower equipment costs [7,9].

The 316L stainless steel is a common material used for many different applications in medical, construction, automotive and chemical industries. It is valued for maintaining strength and corrosion resistance at elevated temperatures and has shown good performance in a variety of different metal injection molding (MIM) and additive manufacturing (i.e., extrusion additive manufacturing (EAM)) techniques [7,8,10–17].

The nature and composition of a metal–binder slurry is selected based on interactions between the metal and the binder as well as the effectiveness of the debinding process. Most binders are composed of a primary binder and a secondary binder. The primary binder is easily removed at a low temperature and opens up a large network of pores in the part. The secondary binder remains to help maintain the structure of the part until a final thermal treatment. During this treatment, it escapes using the network left by the primary binder by evaporation or reactions with the atmosphere. The binder commonly used with 316L is a mixture of polypropylene, paraffin wax, and stearic acid [8,18,19]. This system is based on the original binder systems developed in the beginning of MIM. Paraffin wax functions as the primary binder. It helps give the paste good flowability and it can be easily removed with a hexane solvent. The stearic acid functions as a surfactant to improve the effectiveness of the paraffin wax and is also removed by hexane. The secondary binder is the polypropylene. It remains in the part after solvent debinding and helps maintain the structure of the part. It is removed by thermal treatment during an intermediate stage of the final sinter [19].

The binder used in this study is a water-based methylcellulose gel. In this case, the primary binder is water. Water assists in the flowability and is then readily removed through a drying process via evaporation. The secondary binder, methylcellulose, is then removed using a thermal treatment. Organic water-based systems are seen as simple and cost-effective. Methylcellulose is also an inexpensive, environmentally friendly, safe compound. Studies have found it to be an effective binder for many different AM applications [20]. Research has not been found using the methylcellulose–316L system, but studies have shown efficacy with the methylcellulose–copper (Cu) system.

To attract companies unequipped for powder metallurgy processing, priority is given to studies that can limit any capital investment. While research has been conducted on printing 316L using EAM and MIM processes [7,8,10], this printing occurs with wax-based binders which involve debinding steps with hazardous hexane or heptane solvents. Traditional sintering temperatures for 316L powder are also high, close to 1400 °C under pure hydrogen atmosphere. This is beyond the capacity of common industrial furnaces, and it requires infrastructure to support a dangerous, flammable gas.

Studying the debinding thermal treatment involves manipulating the temperature, dwell time, heating rate, furnace atmosphere, and gas flow rate. When working with 316L, it is critical to bear in mind that this is a low-carbon (C) austenitic stainless steel with a maximum C content of 0.03 wt.%. For some materials, a small added C content of 0.1 wt.% would be unimportant. With 316L, any C remaining in the material can diffuse and form Cr carbide which will dramatically decrease corrosion resistance. This makes this step particularly important for stainless steel [21].

The sintering temperature for 316L powders for optimal densification is between 1250–1380 °C [22] and is driven by supersolidus liquid phase sintering. The 316L forms a partial liquid phase which assists in the densification of the powder by improving the rate of particle rearrangement and improving the rate of particle distortion through solution–reprecipitation. Conversely, persistent liquid phase sintering is a process that introduces a foreign metal that forms the liquid phase at that metal's melting point [23]. It has the same function as the partial 316L liquid phase, but it allows for sintering at lower temperatures and persists in the matrix after cooling. This process has resulted in large decreases in sintering temperatures for systems like Ni–W and WC–Co [24,25].

Cu has a melting point of 1083 °C; 8–10 wt.% Cu will diffuse into an FCC Fe matrix at 1200 °C, and beyond this it will form a partial liquid phase to assist with sintering. Cu diffuses up to 8–10 wt.% in an Fe matrix, and it would partially dissolve Fe and Cr. It is also completely soluble in nickel (Ni).

While a good deal of research has been conducted on printing 316L using EAM and MIM processes, most studies involve debinding steps with hazardous hexane or heptane solvents. Sintering temperatures for 316L powder are also above 1200 °C and close to 1400 °C under pure hydrogen atmosphere. In order to undergo those specific conditions, this paper studies variations in the post treatment of 316L extruded parts. It tries to eliminate the need for the solvent debinding step by using methylcellulose as an alternative binder. It also explores sintering 316L at a lower temperature of 1200 °C by adding Cu to function as a persistent liquid phase [26]. Lastly, it removes pure hydrogen from the debinding and sintering steps to study using safer gases like argon, Ar/5%H_2, and Ar/1%O_2. Argon has been used as an effective debinding gas in various applications while the Ar/5H_2 functions as a reducing gas for oxides, and Ar/1%O_2 can help fully remove C through oxidation.

2. Materials and Methods

2.1. Creating the Organic Paste and Printing

Obtaining parts by AM by material extrusion requires that the feedstock exhibit appropriate rheological behavior throughout the shaping stage. During extrusion, the material will undergo an intense shear gradient going from zero shear, corresponding to the state of rest in the packaging container, to high shear as it passes through the nozzle and finally shear weak gravity induced on the extruded bead. The rheological properties that govern these transitions are material viscosity, viscoelastic modulus, viscosity recovery behavior, and shear stress. From an experimental point of view, the higher the viscosity of a system, the higher the fidelity during deposition and the better the shape retention properties after extrusion. A material exhibiting ideal behavior must therefore have a low viscosity for shear rates (corresponding to the conditions of the extrusion shaping step) and a sufficiently high viscosity at rest (zero shear) to limit the deformation of the structure. The pastes fabricated in this study have those particular behaviors. Printing parameters can be found in Table S1.

A gas-atomized 316L stainless steel with d_{50} of 12 μm and D_{90} of 23 μm was used for this study. Gas-atomized Cu with d_{50} of 9.5 μm and D_{90} of 18 μm was also used (cf. Figure 1). Both materials were supplied by SAT Nano Technology Material Co., Ltd. Both types of particles had a uniform, spherical shape. Powder composition is reported in Table 1. The methylcellulose used was Methocel® A4M, purchased from Sigma-Aldrich. The primary binder was water with 8 wt.% methylcellulose added to form a gel. This binder was mixed with 45 vol.% 316L particles and Cu amounts varying between 0, 10, and 20 vol.%. Cu and 316L powders were mixed prior to inclusion of the binder. All mixing was performed using a THINKY ARE-250 conditioning mixer (THINKY Corporation, Tokyo, Japan). To evaluate printability of the pastes, printing was conducted using a Lynxter S600D professional 3D printer (Lynxter, Bayonne, France) with a PAS11 toolhead.

Paste compositions were successfully printed into 1 cm³ cubes, but after evaluation, the samples contained large air pockets. These air pockets were related to the relaxation of the paste and insufficient degassing processes. These air pockets were expected to cause large deviations in densification measurements, so the paste was instead deposited into silicone molds to form bars (length: 10 cm; thickness: 0.90 cm).
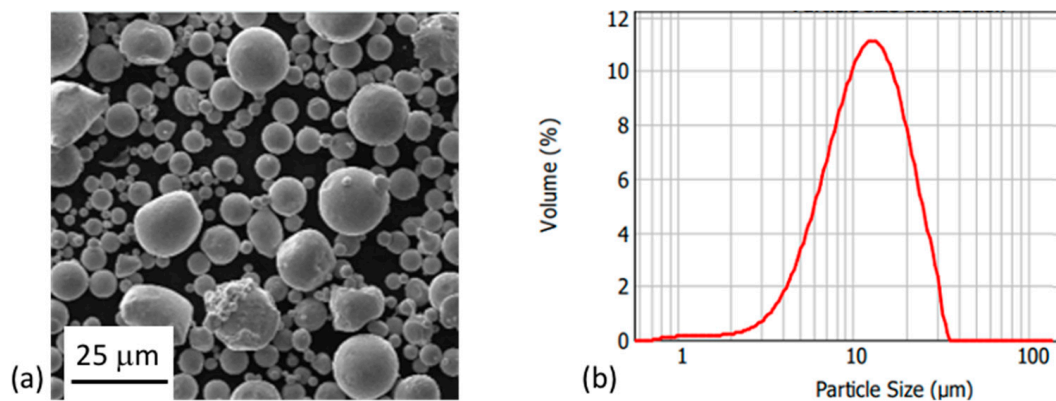
Figure 1. (**a**) SEM micrograph of 316L particles formed by gas-atomization. (**b**) Particle size distribution of those 316L particles.

Table 1. Chemical composition of the 316L powder.

wt.%	Cr	Ni	C	Mn	Mo	Si	P	S	Fe
316L spec.	16–18	10–14	0.03 max.	2.00 max.	2.0–3.0	1.00 max.	0.045 max.	0.030 max.	Bal.
Material used	17.30	12.23	0.017	0.08	2.17	1.00	0.014	0.002	Bal.

2.2. Debinding

The bars were placed in semicylindrical alumina crucibles and debinded using a tubular furnace (Beijing JinYeHong Metallurgical Mechanical Equipment Corp Ltd., Beijing, China). To determine a debinding process sufficient to remove the binder, several different atmospheres, temperatures, and dwell times were evaluated. Argon (Ar), Ar/5%H_2, and Ar/1%O_2 were all tested between 400–700 °C with dwell times from 30 min to 10 h. Temperature heating rates were 3 °C/min. Results showed insufficient carbon (C) removal under argon and Ar/5%H_2 atmospheres across all temperatures and dwell times with retained C measuring from 0.117–0.127 wt.% C.

An Ar/1%O_2 step was added to encourage the removal of C through oxidation. This gas composition was chosen because it is readily available in the industry. There was concern of overoxidation of the material, so temperatures and dwell times were tested to find an optimal quantity to remove the C and minimize 316L oxidation. Oxidation was evaluated using oxygen content measurements. This favored a dwell time of 180 min at 475 °C to yield the lowest oxygen content and still bring the C content to a maximum of 0.032 wt.%.

To minimize the oxygen content in the samples, debinding was first performed under Ar/5%H_2 at 500 °C for 5 h, and then the Ar/1%O_2 step was performed at 475 °C for 3 h.

2.3. Sintering and Hot Rolling

For sintering, the samples were brought to 1200 °C at 3 °C/min under Ar/5%H_2 atmosphere to reduce the oxides on the material before densification. This was performed as a possible nonflammable alternative in place of pure hydrogen. Samples had dwell times of 5 and 10 h. Long dwell times are required to offset the decrease in temperature. Samples were then left to cool in the furnace overnight. Prior to any analysis, samples were mirror-polished on each side. The dimensions of the tested materials (316L, 316L + 10% Cu, and 316l + 20% Cu) were 50 mm × 10 mm and 5 mm in thickness after polishing.

Hot-rolled materials were placed in an oven (Beijing JinYeHong Metallurgical Mechanical Equipment Corp Ltd., Beijing, China), under neutral atmosphere, for 30 min at 500 °C, according to Y. Dong et al. [27], and then immediately hot-rolled (Cavallin 130 mm Rolling Mill (Beijing JinYeHong Metallurgical Mechanical Equipment Corp Ltd., Beijing, China) at a speed close to 10^{-2} m/s. The temperature of the roller close to 100 °C was measured by

thermocouple (Prosensor, Amanvillers, France) just prior to hot rolling. Each pass induced a thickness reduction of 10%.

2.4. Methods

Densification measurements were taken using the Archimedes method in water. Samples were mounted and polished to 1 μm using a diamond suspension. Ferric chloride and aqua regia etchants were attempted on samples to reveal the stainless steel particle grain boundaries, but these would overetch the Cu, so were not used. Samples were left unetched and were analyzed using scanning electron microscopy (SEM, Tescan, VEGA © II SBH, Brno, Czech Republic) and energy-dispersive x-ray spectroscopy (EDS) (Bruker, Billerica, MA, USA).

Carbon contents were measured using a CS800 carbon–sulfur determinator (ELTRA®, Carbon analyzer CS-2000, Haan, Germany). Initial carbon content for the 316L powder was 0.0301 wt.% +/− 0.002.

Hardness values are averages of 10 measurements determined by indenting a pyramidal diamond piece with force of 5 kgf (49 N) during 15 s, on a polished surface (WILSON Hardness, Vickers 452 SVD, London, UK).

Mechanical properties of the materials were determined by the ultrasound method (homemade apparatus) This method makes it possible to measure the speed of propagation of longitudinal v_L and transverse v_T waves in a homogeneous, isotropic, and nondispersive material with density ρ. The measurement is carried out by transmission and requires a transmitter and a receiver including a longitudinal wave probe and a transverse wave probe. They will propagate an ultrasonic wave from its surface and determine the speeds v_L and v_T according to the ratio between the thickness e of the material and the transit time t of the ultrasonic wave [28]. The ultrasonic attenuation in the 316L and 316L + Cu samples was measured by pulsed-echo ultrasonic method as per ASTM E664/E664M-10: standard practice for the measurement of the apparent attenuation of longitudinal ultrasonic waves work [29]. A schematic representation of the ultrasonic method is shown in Figure S1.

To compare corrosion resistance, samples were placed in a 5% HCl aqueous solution for 84 h and a corrosion rate was measured.

3. Results

3.1. Material Deposition

Paste compositions were chosen through investigation. The 316L metal content had a larger impact on the printability of the paste than the Cu content. The methylcellulose–316L paste had a uniquely thick, sticky texture. The 316L content was held constant and the total metal loading was adjusted so that all compositions could be printed. The 45 vol.% 316L showed the best results and allowed sufficient printability for the deposition of all the Cu contents. For these compositions, the 316L and 316L + Cu pastes showed a shear thinning behavior which is suitable for an extrusion shaping process.

Pastes were printed into 1 cm³ cubes formed with uniform extruded pipes, as shown in Figure 2a. One consequence of the sticky paste formulation is the prevalence of air bubbles within the paste. Degassing procedures were unsuccessful in removing the air, causing gaps in the paste flow. After the samples dried, cross-sections also showed air pockets within the material, as seen in Figure 2b. These air pockets were found in gaps between the extruded pipes and a large air pocket was found in the center of every sample. The mechanism for this air pocket is unknown.
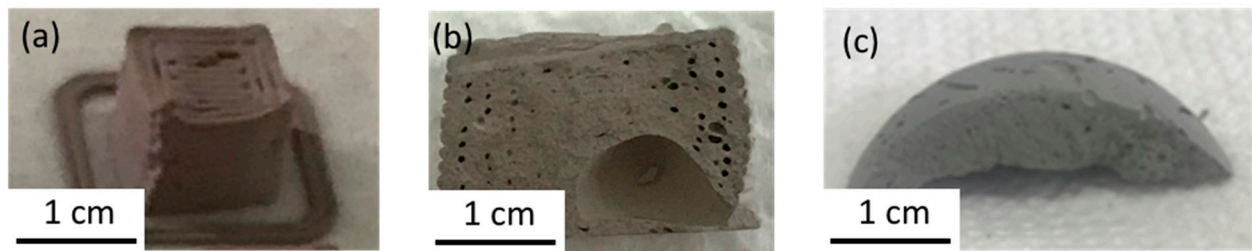
Figure 2. Photographs of (**a**) as-printed sample, (**b**) cross-section of as-printed sample, and (**c**) cross-section of sample formed using a cylindrical mold.

To limit these air pockets, the calendaring process, using silicone molds, provided an alternative that did not result in large gaps within the material. A proper degassing procedure was not successful in preventing air bubbles, so even material formed with molds (cf. Figure 2c) had air pockets, but these were smaller than the printed material. The error caused by these air pockets on the final densification was not quantified. The paste formulations used in this study are extrudable and can be printed into a desired shape. A degassing procedure still needs to be defined and the relaxation of the paste needs to be improved to decrease the initial porosity.

3.2. Debinding

Initial debinding trials were conducted on 316L samples with no Cu addition. Debinding was initially tested under argon and $Ar/5\%H_2$ atmospheres. Thermogravimetric analysis shows that methylcellulose fully degrades between 450–500 °C (cf. Figure S2). Temperatures tested were 400, 500, and 700 °C, with dwell times varying from 90 to 900 min. Heating rates were 2 °C/min and samples were cooled in the furnace overnight. Results are shown in Table 2. The lowest C content was 0.117 wt.%, achieved when the debinding was conducted at 700 °C in $Ar/5\%H_2$ for 300 min. During the C content determination, error for these values were seen as high as $+/- 0.002$ wt.%, so conclusions on trends cannot be made without more trials.

Table 2. C contents after debinding under various atmospheres, temperatures, and dwell times.

Gas Composition		Temperature	Dwell Time	Carbon Content
Argon (%)	H$_2$ (%)	(°C)	(min)	(wt.%)
316L powder (as received)				0.03
100	0.0	400	90	0.130
100	0.0	500	90	0.127
100	0.0	500	300	0.125
95	5.0	500	300	0.125
95	5.0	500	900	0.123
100	0.0	700	300	0.122
95	5.0	700	300	0.117

For debinding at 500 °C, C soot was visible on the surface. Debinding at 500 °C is sufficient to degrade the methylcellulose, but this atmosphere does not effectively remove the C. While 700 °C showed the best C removal, the material had a hard, dark surface with no visible soot or debris. Backscattering micrographs show dark particles and some oxide growth on the sample treated at 700 °C. EDS analysis also shows the presence of a thick Cr oxide on the surface. This oxide may be formed by the reaction of the Cr with the oxygen of the methylcellulose during degradation. The higher temperature promotes this reaction. It is also suspected that the hardness of the samples is related to C diffusion within the sample, causing the formation of Cr carbides. This was not confirmed, but it would

negatively impact the corrosion resistance, and would make C removal more difficult. To prevent these things from occurring, the temperature for subsequent thermal treatments was kept at 500 °C.

Large increases in dwell time may result in improved C removal, but excessively long dwell times become impractical for industrial application. Instead, the decision was made to use an oxidizing atmosphere at a lower temperature to remove the remaining C. Heat treatments were conducted at a constant dwell time for different temperatures. The amount of oxidation was measured by determining oxygen contents after treatment. The C content was also measured to determine the amount of removed C. The samples were placed under $Ar/1\%O_2$ for 180 min. Results for different temperatures are shown in Figure 3.
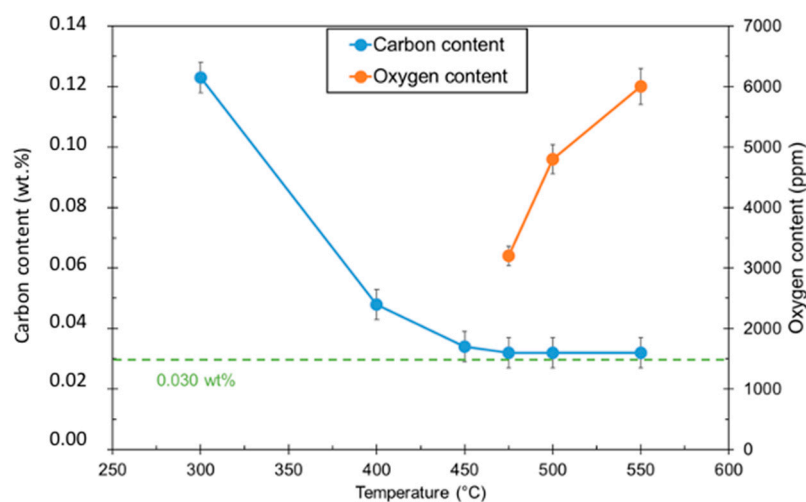

Figure 3. Carbon and oxygen contents of 316L materials after $Ar/1\%O_2$ debinding stage.

C contents show an asymptotic trend, with the C content leveling off at 0.032 wt.% C. For this reason, the temperature chosen for the debinding process was 475 °C. This resulted in minimal oxidation while still achieving the maximum observed C removal.

3.3. Sintering

After debinding, the sintering of the samples with different Cu contents was studied. This was carried out through studying the microstructure, the mechanical properties, and the corrosion properties of the samples. Samples had visual appearances which varied dramatically with the Cu content, as shown in the Supplementary Material Figure S3. All samples containing Cu showed an area at the bottom of the samples where some liquid Cu melted and pooled. All the samples also had a dark green surface on the top and the sides. XRD conducted on these samples showed a large quantity of Cr and silicon oxide on the surface which corresponded to a green color. Only 1 wt.% silicon exists in 316L, but silicon oxide will readily form under the oxidizing conditions seen in the $Ar/1\%O_2$ debinding step. One theory for the oxidation was that oxygen from reduced Fe or Cu oxides reacted with Cr to form Cr oxide. Oxygen contents were then measured on samples before and after sintering to compare values.

These numbers showed a large increase in oxygen contents within the sintered samples.

3.4. Densification

Figure 4 shows the relative density as a function of the sintering dwell time and Table 3 shows the corresponding densities. Traditional analyses of densification compare initial and final densities of the different process variables. In this case, the density prior to sintering, or "green" density, was estimated based on the volume fractions of the material and the material's mass. The binder mostly made up of water had only a small methylcellulose content. The green open porosity was also unable to be directly measured because in this

system it was effectively 100%. Many traditional wax-based binders fill gaps between the particles and generate more closed porosity, while low-content binders result in minimal closed porosity. Because of this, direct comparisons before and after sintering are difficult to conduct.
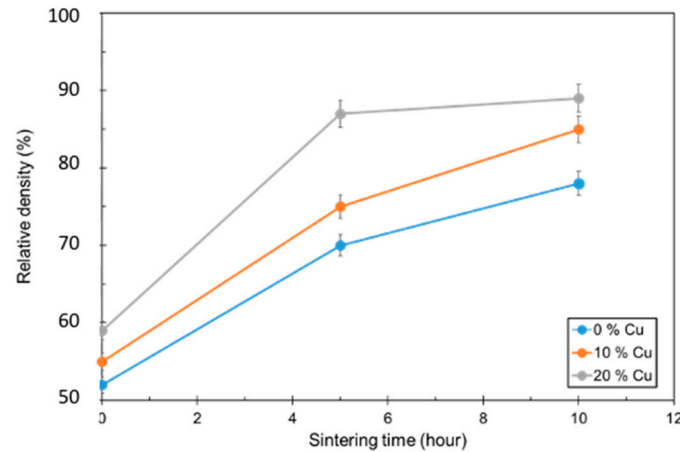

Figure 4. Relative density as a function of sintering dwell time for 0, 10, and 20 vol.% Cu.

Table 3. Relative density and density of 316L, 316L + 10% Cu, and 316L + 20% Cu samples for three annealing times (0 h, 5 h, and 10 h).

		316L	316L + 10% Cu	316L + 20% Cu
0 h	Relative density (%)	52.17	56.10	59.57
	Density (g/cm^3)	4.12	4.43	4.70
5 h	Relative density (%)	70.40	75.65	87.40
	Density (g/cm^3)	5.36	6.05	6.99
10 h	Relative density (%)	80.00	86.10	88.70
	Density (g/cm^3)	6.49	6.98	7.19

Larger Cu contents resulted in higher densification numbers. The 20 vol.% Cu samples were able to achieve 88% densification after sintering for 5 h. The other samples were approaching similar values as the dwell time increased. The 20 vol.% Cu samples also had the lowest amount of open porosity, and this value did not change with longer dwell times.

When looking at the densification rate as a function of dwell time, one can break down the mechanisms of liquid phase sintering. Density increases dramatically due to the rearrangement of atoms and the introduction of the liquid, until eventually leveling off as the process approaches solid-phase sintering. In this case, larger quantities of copper promote a faster rearrangement step and result in a larger increase in density immediately after liquid formation. The 20 vol.% copper also reaches the solid-phase sintering stage where the density is no longer changing dramatically. The 0 and 10 vol.% copper samples have not leveled off yet, so it is supposed that a longer dwell time would contribute to higher densification numbers.

3.5. Microstructure

Etching the samples resulted in preferential overetching of the Cu, so unetched samples were observed under backscattering electron analysis. Figure 5a,c show micrographs of 10 and 20 vol.% Cu samples. Pores are primarily seen within the Cu region instead of within the 316L particles. The primary material seen within the pore sites is silicon oxides, which are highlighted in pink (Figure 5d). It should also be noted that no Cr oxide was observed within the matrix. EDS shows minimal Cu diffusion into the 316L particles, much less than

the 8–10 wt.% expected in the Fe–Cu binary phase diagram (Figure 5b,d). Some Ni and molybdenum were also seen to diffuse into the Cu region.
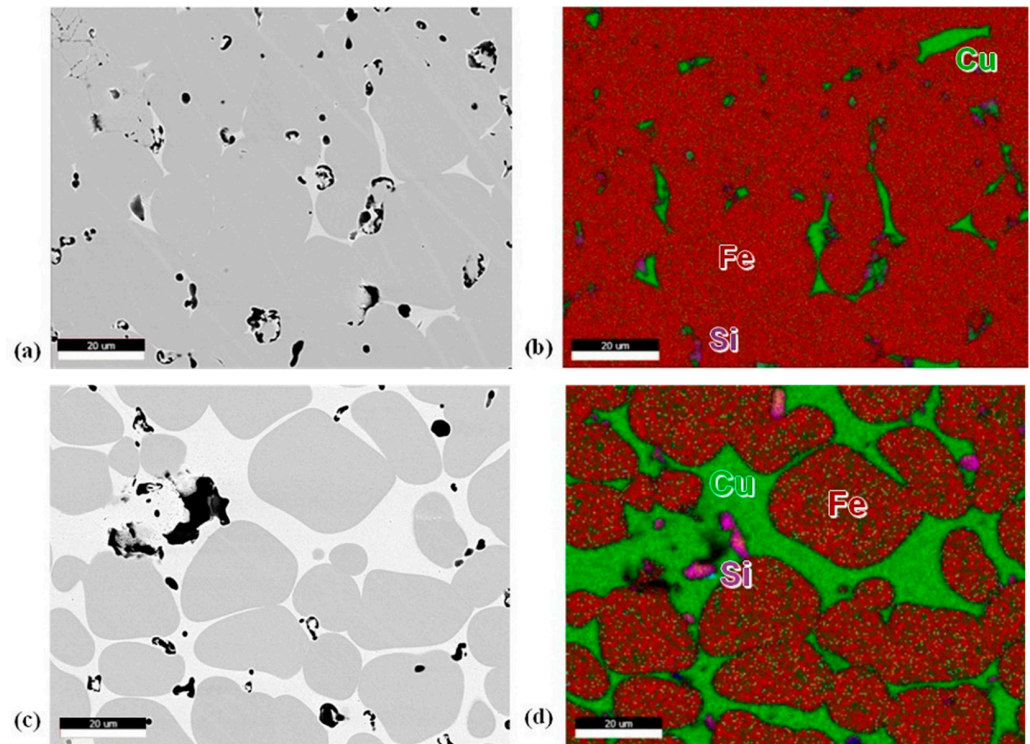

Figure 5. (**a**) 10 vol.% Cu BSE micrograph, (**b**) 10 vol.% Cu EDS map, (**c**) 20 vol.% Cu BSE micrograph, (**d**) 20 vol.% Cu EDS map. For EDS maps, Fe is red, Cu is green, and silicon is pink.

When comparing the 20 vol.% Cu to 0 vol.%, the SEM micrographs in Figure 6 show larger 316L particles in the 20 vol.% Cu material (30% to 50% increase in average size). When referring to the mechanisms for liquid phase sintering, this shows that the Cu is successful in assisting not just the rearrangement of the 316L particles, but particle growth as well.
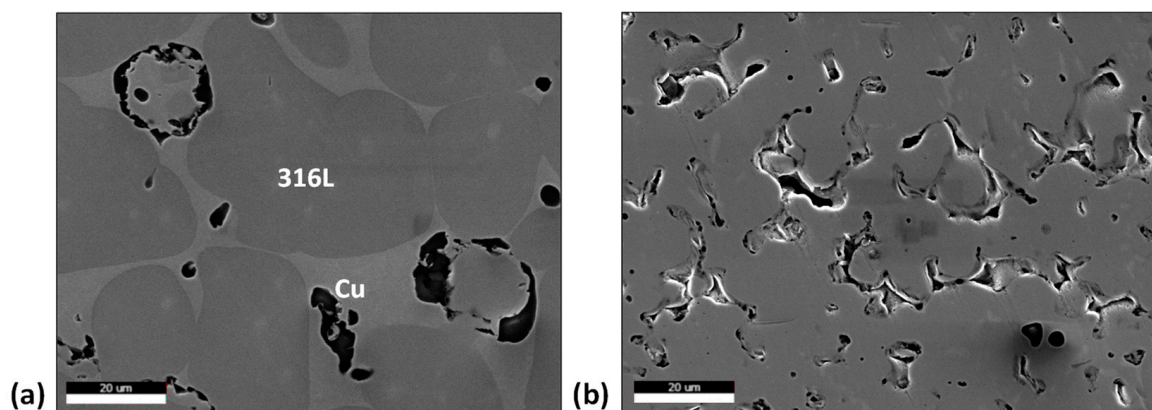

Figure 6. SEM micrographs for (**a**) 20 vol.% Cu, (**b**) 0 vol.% Cu.

The XRD diffractogram shows the presence of a single phase with peaks corresponding to the austenite phase (cf. Figure S4). The initial 316L powder showed mostly the FCC austenite phase with some BCC delta ferrite phase. Different quantities of the alloying elements promoted either the FCC or BCC phase.

The addition of Cu promoted the FCC phase, and after treatment, no BCC phase was seen in the material. The XRD diffractogram shows a clear FCC structure. When Ni diffuses

into Cu, the unit cell parameter for the FCC Cu phase is similar to the austenite unit cell, so it only appears as a single phase within the spectrum.

3.6. Mechanical Properties

Vickers hardness results are shown in Figure 7. They show an increase with increasing Cu content that levels off at 20 vol.% Cu and an HV of about 92. Because these values correspond well with the densification values, it was theorized that the increased hardness values are simply due to changes in the densification more than the presence or absence of Cu. To investigate this theory, samples with 20 vol.% Cu were hot-rolled to mechanically reduce the porosity and then subsequently heat-treated. The densification of these samples increased to 94% and the resulting hardness was 150 HV. This shows that improvement of densification will result in a large improvement of mechanical properties. It also shows that the densification will need to be improved to properly compare the effects of Cu additions to standard stainless steel. With this current process, the hardness values fall short of the 316L ASTM standard of 220 HV.
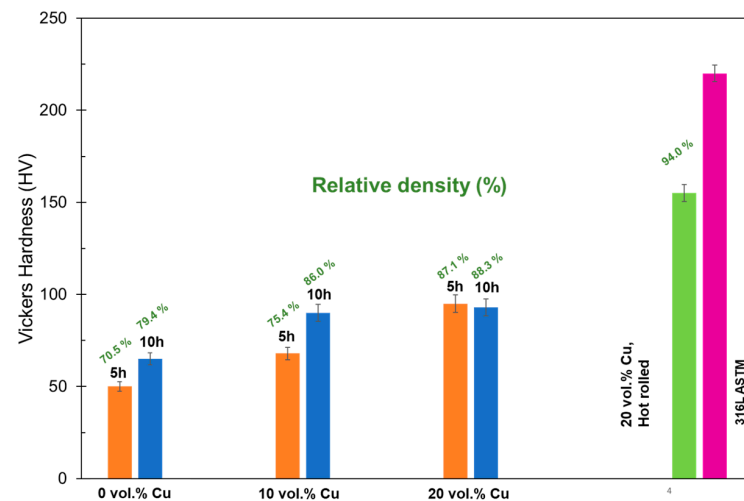

Figure 7. Hardness values for different Cu compositions, after sintering for 5 and 10 h.

The yield strength for the material was estimated using an ultrasonic method and compared to a sample of pure 316L. Results are shown in Figure 8. They show a similar trend with the highest yield strengths found for the largest Cu contents. They also show a consistent decrease in yield strengths for the longer sintering dwell times. These are closer, but still fall short of the minimum 170 MPa requirement for 316L.
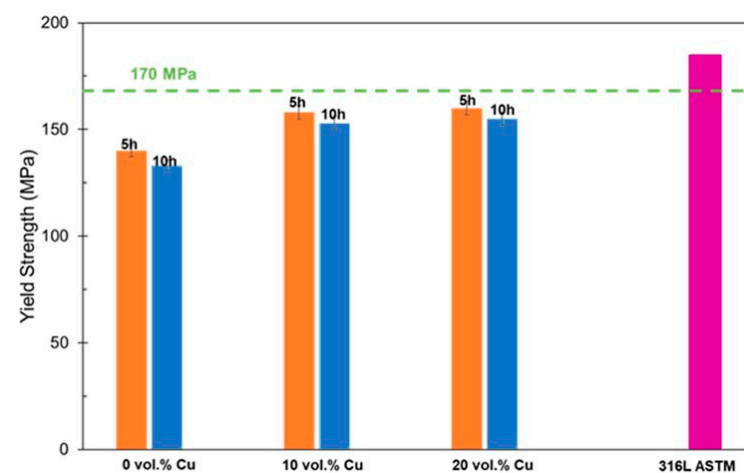

Figure 8. Yield strengths for different compositions for two sintering durations.

3.7. Corrosion Properties

There are many different mechanisms for different types of corrosion in stainless steel. The most common environment studied is using a chloride-bearing aqueous solution similar to seawater. The 316L, because of its chromium (Cr) and molybdenum (Mo) contents, is often a desired choice for seawater applications. Even so, the seawater environment will still initiate pitting and crevice corrosion in 316L. These can be difficult to detect because this type of corrosion creates large cavities which are deep within the material and are only visible as small pits on the material surface. Chlorine ions lead to oxidation of the solid iron (Fe) and form an anodic site surrounded by normal material which functions as a cathode (O$_2$ reduction).

Corrosion of the 316L samples was evaluated by exposing them to a chloride-bearing environment. Samples were placed in a 5% HCl aqueous solution, and masses were measured gradually over the course of 84 h. This is a process that was performed in a study by He et al. [30], and the results were then compared to the results found in that study. That study achieved 93 and 98% densification. The corrosion rate of the material was then calculated using the following formula:

$$\text{Corrosion rate} = \text{Mass loss}/(\text{Sample area} \times \text{Time}) \qquad (1)$$

Results are shown in Table S2. The pure 316L material showed the highest corrosion rate. Flaking was seen on these samples during the corrosion testing which resulted in large mass drops. The corrosion rate was the lowest for the largest Cu content, i.e., 20 vol.%.

4. Discussion

Sintering is conducted under a reducing atmosphere with argon and hydrogen. The reduction of oxides will depend both on the temperature and on the amount of available oxygen. With stainless steel sintering, this is quantified by the dew point. The dew point is related to the ratio of hydrogen to water. A curve summarizing the reduction of Si and Cr oxides is shown in Figure S5. This shows two different dew points resulting in oxide reduction at very different temperatures. Proper sintering of 316L is traditionally performed above 1000 °C with a pure hydrogen atmosphere and a dew point of less than −40 °C [24]. At 1200 °C, Figure S5 shows that the dew point must be less than −20 °C to reduce Cr. Based on gas tank specifications, the inlet gas has a theoretical dew point of −38 °C, but this value has not been confirmed within the furnace itself. When the material is heated to 1200 °C, three major steps occur. The Cu melts at 1083 °C, the Cr oxide reduces, and the silicon oxide reduces. Ideally, both oxides will reduce before melting of the Cu. This would limit the amount of oxygen within the matrix when the sintering starts. At a dew point of −38 °C, the Cr reduces, but it is unclear if the silicon does. After sintering, the material is slowly cooled to room temperature. As the temperature passes below the oxidation temperatures, the Cr and Si on the surface begin to oxidize, and after a long cooling time, the result is a large oxide layer seen on the final part.

Within the sample, the EDS analyses showed that the pores contain large quantities of silicon oxide and no Cr oxide at all. This confirms that the Cr oxide reduces, and any oxygen retained in pores forms silicon oxide. The silicon oxide contents are not seen uniformly in all the pores, so it is not entirely clear if the silicon is reducing at all. Either way, the amount of oxide found in the Cu liquid before reducing will harm the densification of the final material. If the dew point is less than −38 °C, this may affect this quantity. Drops in dew point could be caused by leaking within the furnace, inadequate drying or purging before processing, or higher oxygen contents in the inlet gas. Ultimately, silicon oxide is also undesirable because silicon on the surface is shown to promote pitting corrosion in 316L. To ensure these oxides are reduced, methods must be pursued to manage the dew point and to minimize oxidation after sintering through a faster cooling process. The literature also shows that low cooling allows greater growth of Cr carbides, which has an additional negative effect on corrosion, although it must be noted that this conclusion has not been

confirmed with analysis. Because of this effect, most stainless-steel processes require the use of a water or salt quench as the preferred cooling method.

It is hard to compare our results obtained by AEM using bio-sourced paste with 316L materials from the literature due to the fact that base materials, and debinding and sintering conditions are different. Table 4 shows a comparison of 316L materials fabricated using Direct Laser Deposition (DLD), SLM, MIM and EAM with our materials. It has to be mentioned that literature materials are pure 316L where Cu can be added to our 316L in order to improve densification and that 316L materials from the literature are sinter at high temperature (close to 1400 °C) where our materials are sinter at much lower temperature (1200 °C).

Table 4. Overview of mechanical properties and porosity for 316L and 316L + Cu samples produced using fused filament fabrication (FFF), SLM, and MIM.

Porosity (%)	Hardness	Yield Strength	Method	Reference
<0.5	240 HV	2200 MPa	DLD	[31]
	380 HV	2300 MPa	SLM	
-	213 HB	375 MPa	SLM EOS	[32]
-	217 HB	533 MPa	SLM Renishaw	[32]
10	126 HB	153 MPa	FFF BASF	[32]
4	-	170 MPa	MIM	[33]
1.6	200 HV	-	EAM	[34]
~21	65	140 MPa	EAM 316L	
~14	85	150 MPa	EAM 316L + 10% Cu	This work
~12	85	150 MPa	EAM 316L + 20% Cu	

4.1. Densification

When looking at the densification rate as a function of dwell time, one can return to the stages of liquid phase sintering, as shown in Figure S4. The density increases immediately due to the rapid rearrangement of atoms with the introduction of the liquid. Particle distortion and atom reprecipitation occur at a slower rate, until the densification of the system levels off. Higher liquid contents show sharper density increases initially due to more liquid assisting the rearrangement phase. The 10 vol.% Cu sample showed a much more gradual leveling off because it was more dependent on the solution reprecipitation phase. The particles required more distortion to reach the same density as the 20 vol.% Cu which increases the required dwell time. The 0 and 10 vol.% Cu samples had not leveled off at 10 h, so it is supposed that a longer dwell time would contribute to higher densification numbers. It is not clear if these numbers would be higher than the 88% found with 20 vol.% Cu, but yield strength measurements suggest that longer dwell times will negatively affect mechanical properties. Traditionally, final densification is directly connected to the temperature and the dwell time. Lower temperatures require longer dwell times. Dwell times that are too long will cause the material to soften; so, to minimize this, the temperature needs to be increased. One sees a similar relationship with Cu contents. Higher Cu contents result in shorter dwell times, but they are leveling off at a low densification.

Strong capillary forces between the liquid Cu and the 316L particles cause the Cu to penetrate in between the particles, leaving pores behind. Some studies on high-density Fe–Cu compacts have shown particularly aggressive penetration along grain boundaries that can cause a geometric swelling of the material. Large initial porosity prevents this swelling and studies have also shown that Cu's aggressive penetration can actually be useful in filling larger pores [28,35,36]. Studies also show that the addition of C in the Fe matrix helps to minimize Cu diffusion and material swelling. The low Cu contents found within the 316L particles supports these studies. Specific mechanisms for explaining the retained porosity cannot be determined currently.

4.2. Mechanical Properties

The hardness tests correlated the densification closely, so conclusions on mechanical behavior from these values were impossible. The yield strength measurements provided more insight. There was a slight increase in the yield strength with the Cu content, and, like the hardness, it is unclear if this was caused by the addition of Cu or the densification. All samples, however, showed a marked decrease in strength at 10 h when compared to 5 h. As the material coarsens, the density does increase, but the material also softens as the particles combine and the average grain size increases. This softening overtakes the densification to negatively impact the mechanical properties. While sufficient densification may be achieved at longer dwell times, this may also produce a soft, weak material.

4.3. Corrosion Properties

When observing corrosion properties, one must comment on the large quantities of Cr and Si oxides seen on the surface of the material. Pitting corrosion is activated when there is an unexpected fracture or penetration of the Cr oxide layer. There is a random nature of these occurrences which makes the mechanism for these fractures not fully clear in the literature, but they do occur on the surface of the 316L and result in this type of corrosion. It has also been shown that silicon oxides increase the rate of pit activation under a ferric chloride corrosion environment [37]. Once the Cr oxide layer is broken, the low Cr content in the underlying metal will result in more rapid corrosion within the material. In addition to this, if customers wish to clean or further process the densified parts for their application, the cleaning or mechanical removal of this layer will unveil a material with decreased corrosion resistance.

When looking at the corrosion rates, several different mechanisms are working at once. Cu is more prone to corrosion in chloride-bearing environments then 316L. For example, a common etchant for pure Cu is ferric chloride salt. At the same time, greater porosity results in exponential increases in surface area. The data show that Cu additions may have a positive effect on chloride corrosion resistance, but the 316L samples are also much more porous than the samples with liquid Cu. This higher surface area will result in higher corrosion rates. If the actual sample surface area is inaccurate, the corrosion rate will be flawed.

It should also be said that the effect of Cu on the final corrosion properties will be different in different acidic environments like nitric or sulfuric acids. In sulfuric environments, for example, Cu alloying has been shown to improve corrosion resistance through the formation of stable Cu sulfides [17]. These sulfides function similarly to Cr oxide to form a stable protective layer on the surface and protect the stainless steel from forming the pits seen in pitting corrosion. Thus, depending on the application of the material, its corrosion resistance must be measured and evaluated differently.

5. Conclusions

This study investigated the use of methylcellulose–water gel as a binder for 316L powder. It studied effective debinding methods and pursued a low-temperature sintering process. The paste formed with this binder had adequate flow characteristics to successfully print parts that retained their structure. These parts had some difficulty with air pockets which forced the use of a different method for the creation of samples.

The binder was then successfully removed prior to sintering by using a two-step thermal treatment process. The first one used an $Ar/5\%H_2$ atmosphere to degrade the methylcellulose to C. The second one was performed under $Ar/1\%O_2$, which oxidized the C to decrease C contents down to 0.032 wt.% C. Values under that could not be achieved due to C diffusion into the 316L. This provides a safer, environmentally friendly alternative to wax-based binders and solvent baths.

Cu was introduced as a possible way to reduce the sintering temperature by using the persistent liquid phase sintering mechanism. The 10 and 20 vol.% Cu samples were studied

and compared to pure 316L powder under the same conditions. Of the samples studied, 20 vol.% Cu sintered for 10 h showed the highest densification, with 88% relative density.

The 20 vol.% Cu sample showed the highest hardness and yield strength. A mechanical decrease in porosity showed a large increase in hardness, which indicates that a higher density will have a dramatic effect on mechanical properties. The yield strength decreased with longer dwell times, showing that the pursuit of maximum densification will result in the compromise of the mechanical properties. Caution must be taken in the future to minimize dwell times.

Conclusions on the corrosion properties were unable to be determined. Low densification results in a high surface area which will damage corrosion resistance. It is also likely that the addition of Cu harms corrosion resistance, but no clear trends were seen.

Sintering was conducted under $Ar/5\%H_2$ instead of pure H_2. There was successful reduction of the Cr oxide, but it is unclear if the Si oxide reduced before the Cu melted. Cr oxide was not found within the sample, but silicon oxide was located within the pores of the material. Any unreduced oxide within the liquid can promote the formation of pores upon reduction. These oxides may need to be reduced to obtain adequate densification. Increases in the hydrogen ratio of the $Ar/5\%H_2$ gas may also be sufficient to reduce these oxides. Finding and eliminating sources of moisture in the furnace may minimize these oxides as well. During slow cooling, a large layer of Cr and silicon oxides is formed on the surface. The effect of rapid cooling rates on the oxide layer and the corrosion resistance may be significant and is worth studying.

Excessive pores may also be the result of insufficient liquid amounts. One study showed that a content of 25 vol.% Cu was required to obtain adequate densification properties [16]. It also included an addition of tin, which the study stated improved the mechanical properties. A study of the content and composition of the liquid can be continued.

Adequate densification has not yet been achieved to yield competitive properties. Even so, this first step showed that methylcellulose may be used as an effective binder for 316L. It also showed that after some development and increased densification, Cu additions may be an effective option to apply extrusion additive manufacturing techniques to the creation of competitive 316L parts.

References

1. Liu, B.; Wang, Y.X.; Lin, Z.W.; Zhang, T. Creating metal parts by Fused Deposition Modeling and Sintering. *Mater. Lett.* **2020**, *263*, 127252. [CrossRef]
2. Spencer, O.; Yusuf, O.; Tofade, T. Additive Manufacturing Technology Development: A Trajectory Towards Industrial Revolution. *Am. J. Mech. Ind. Eng.* **2018**, *3*, 80–90.
3. Galati, M.; Minetola, P. Analysis of Density, Roughness, and Accuracy of the Atomic Diffusion Additive Manufacturing (ADAM) Process for Metal Parts. *Materials* **2019**, *12*, 4122. [CrossRef] [PubMed]
4. Godec, D.; Cano, S.; Holzer, C.; Gonzalez-Gutierrez, J. Optimization of the 3D Printing Parameters for Tensile Properties of Specimens Produced by Fused Filament Fabrication of 17-4PH Stainless Steel. *Materials* **2020**, *13*, 774. [CrossRef]
5. Suwanpreecha, C.; Manonukul, A. A Review on Material Extrusion Additive Manufacturing of Metal and How It Compares with Metal Injection Moulding. *Metals* **2022**, *12*, 429. [CrossRef]
6. Tosto, C.; Tirillò, J.; Sarasini, F.; Cicala, G. Hybrid Metal/Polymer Filaments for Fused Filament Fabrication (FFF) to Print Metal Parts. *Appl. Sci.-Basel* **2021**, *11*, 444. [CrossRef]
7. Hassan, W.; Farid, M.A.; Tosi, A.; Rane, K.; Strano, M. The effect of printing parameters on sintered properties of extrusion-based additively manufactured stainless steel 316L parts. *Int. J. Adv. Manuf. Technol.* **2021**, *114*, 3057–3067. [CrossRef]
8. Banerjee, S.; Joens, C.J. Debinding and sintering of metal injection molding (MIM) components. In *Handbook of Metal Injection Molding*; Woodhead Publishing: Cambridge, UK, 2019; pp. 129–171.
9. Rane, K.; Strano, M. A comprehensive review of extrusion-based additive manufacturing processes for rapid production of metallic and ceramic parts. *Adv. Manuf.* **2019**, *7*, 155–173. [CrossRef]
10. Thompson, Y.; Gonzalez-Gutierrez, J.; Kukla, C.; Felfer, P. Fused filament fabrication, debinding and sintering as a low cost additive manufacturing method of 316L stainless steel. *Addit. Manuf.* **2019**, *30*, 861. [CrossRef]
11. Gong, H.J.; Snelling, D.; Kardel, K.; Carrano, A. Comparison of Stainless Steel 316L Parts Made by FDM- and SLM-Based Additive Manufacturing Processes. *Jom* **2019**, *71*, 880–885. [CrossRef]
12. Kurose, T.; Abe, Y.; Santos, M.V.A.; Kanaya, Y.; Ishigami, A.; Tanaka, S.; Ito, H. Influence of the Layer Directions on the Properties of 316L Stainless Steel Parts Fabricated through Fused Deposition of Metals. *Materials* **2020**, *13*, 2493. [CrossRef] [PubMed]
13. Damon, J.; Dietrich, S.; Gorantla, S.; Popp, U.; Okolo, B.; Schulze, V. Process porosity and mechanical performance of fused filament fabricated 316L stainless steel. *Rapid Prototyp. J.* **2019**, *25*, 1319–1327. [CrossRef]
14. Alkindi, T.; Alyammahi, M.; Susantyoko, R.A.; Atatreh, S. The effect of varying specimens' printing angles to the bed surface on the tensile strength of 3D-printed 17-4PH stainless-steels via metal FFF additive manufacturing. *MRS Commun.* **2021**, *11*, 310–316. [CrossRef]
15. Suwanpreecha, C.; Seensattayawong, P.; Vadhanakovint, V.; Manonukul, A. Influence of Specimen Layout on 17-4PH (AISI 630) Alloys Fabricated by Low-Cost Additive Manufacturing. *Metall. Mater. Trans. A-Phys. Metall. Mater. Sci.* **2021**, *52*, 1999–2009. [CrossRef]
16. Henry, T.C.; Morales, M.A.; Cole, D.P.; Shumeyko, C.M.; Riddick, J.C. Mechanical behavior of 17-4 PH stainless steel processed by atomic diffusion additive manufacturing. *Int. J. Adv. Manuf. Technol.* **2021**, *114*, 2103–2114. [CrossRef]
17. Rosnitschek, T.; Seefeldt, A.; Alber-Laukant, B.; Neumeyer, T.; Altstädt, V.; Tremmel, S. Correlations of Geometry and Infill Degree of Extrusion Additively Manufactured 316L Stainless Steel Components. *Materials* **2021**, *14*, 5173. [CrossRef]
18. German, R.M. Metal powder injection molding (MIM): Key trends and markets. In *Handbook of Metal Injection Molding*; Woodhead Publishing: Cambridge, UK, 2012; pp. 1–25.
19. Quinard, C.; Barriere, T.; Gelin, J.C. Development and property identification of 316L stainless steel feedstock for PIM and μPIM. *Powder Technol.* **2009**, *190*, 123–128. [CrossRef]
20. Dai, L.; Cheng, T.; Duan, C.; Zhao, W.; Zhang, W.P.; Zou, X.J.; Aspler, J.; Ni, Y.H. 3D printing using plant-derived cellulose and its derivatives: A review. *Carbohydr. Polym.* **2019**, *203*, 71–86. [CrossRef]
21. Heaney, D.F.; Mueller, T.W.; Davies, P.A. Mechanical properties of metal injection moulded 316L stainless steel using both prealloy and master alloy techniques. *Powder Metall.* **2004**, *47*, 367–373. [CrossRef]
22. Müller, L. *Powder Metallurgy Data: Chapter 6 Metal Injection Molding*; Springer: Thale, Germany, 2003; Volume 2A1.
23. German, R.; Suri, P.; Park, S. Review: Liquid phase sintering. *J. Mater. Sci.* **2009**, *44*, 1–39. [CrossRef]
24. ASM Committee. *ASM Handbook*; ASM International: Almere, The Netherlands, 1992.
25. Do Kim, Y.; Ryu, S.; Moon, I. Application of Metal Injection Molding to W-Ni-Fe Heavy Alloy. *J. Jpn. Soc. Powder Powder Metall.* **1999**, *46*, 893–897. [CrossRef]
26. Jamil, S.; Chadwick, G. Investigation and analysis of liquid phase sintering of Fe—Cu and Fe–Cu–C compacts. *Powder Metall.* **2013**, *28*, 65–71. [CrossRef]
27. Dong, Y.; Zhang, Z.; Yang, Z.; Zheng, R.; Chen, X. Effect of annealing temperature on the microstructure and mechanical properties of high-pressure torsion-produced 316L stainless steel. *Materials* **2022**, *15*, 181. [CrossRef] [PubMed]
28. Tessier-Doyen, N. Etude Experimentale et Numerique du Comportement Thermomecanique de Materiaux Refractaires Modeles. Ph.D. Thesis, Universite de Limoges, Limoges, France, 2003.
29. Aghaie-Khafri, M.; Honarvar, F.; Zanganeh, S. Characterization of grain size and yield strength in AISI 301 stainless steel using ultrasonic attenaution measurements. *J. Non Destruct. Eval.* **2012**, *31*, 191–196. [CrossRef]

30. He, H.; Li, Y.; Li, D. Effect of sintering temperature and atmosphere on corrosion behavior of MIM 316L steel. *Adv. Mater. Res.* **2011**, *239–242*, 132–136. [CrossRef]

31. Bedmar, J.; Riquelme, A.; Rodrigo, P.; Torres, B.; Rams, J. Comparison of Different Additive Manufacturing Methods for 316L Stainless Steel. *Materials* **2021**, *14*, 6504. [CrossRef]

32. Kedziora, S.; Decker, T.; Museyibov, E.; Morbach, J.; Hohmann, S.; Huwer, A.; Wahl, M. Strength Properties of 316L and 17-4 PH Stainless Steel Produced with Additive Manufacturing. *Materials* **2022**, *15*, 6278. [CrossRef]

33. Zhang, Y.Y.; Feng, E.S.; Mo, W.; Lv, Y.H.; Ma, R.; Ye, S.L.; Wang, X.G.; Yu, P. On the Microstructures and Fatigue Behaviors of 316L Stainless Steel Metal Injection Molded with Gas- and Water-Atomized Powders. *Metals* **2018**, *8*, 893. [CrossRef]

34. Spiller, S.; Kolstad, S.O.; Razavi, N. Fatigue behavior of 316L stainless steel fabricated via Material Extrusion Additive Manufacturing. *Eng. Fract. Mech.* **2023**, *291*, 544. [CrossRef]

35. Lawcock, R.; Davies, D. Effect of carbon on dimensional and microstructural characteristics of Fe–Cu compacts during sintering. *Powder Metall.* **1990**, *33*, 147–150. [CrossRef]

36. Yang, X.; Bai, Y.L.; Xu, M.; Guo, S.J. Effect of Additive Cu-10Sn on Sintering Behavior and Wear Resistance of 316L Stainless Steel. *J. Iron Steel Res. Int.* **2013**, *20*, 84–88. [CrossRef]

37. Kim, S.T.; Park, Y.S. Effect of copper addition on corrosion behavior of high-performance austenitic stainless steel in highly concentrated sulfuric acid solution-Part 1. *Corrosion* **2007**, *63*, 114–126. [CrossRef]